Chair of Automatic Control

Technical University of Munich

Tobias Egle (03665705)

Whole-body Joint Friction Modeling in a Torque-controlled Humanoid Walking Robot

An acceleration-based approach

Term paper (Semesterarbeit)

Supervisor(s): PD Dr.-Ing. habil. Paul Kotyczka
Chair of Automatic Control
Prof. Dr.-Ing. Alin Albu-Schäffer
German Aerospace Center, Institute of Robotics and Mechatronics

Advisor(s): Dr.-Ing. Johannes Englsberger
George-Adrian Mesesan, M.Sc.
Robert Schuller, M.Sc.

Submission date: 17 February 2021

Erklärung

Ich versichere hiermit, dass ich die von mir eingereichte Arbeit selbstständig verfasst und keine anderen als die angegebenen Quellen und Hilfsmittel benutzt habe. Mit der zeitlich unbefristeten Aufbewahrung und Bereitstellung meiner Arbeit in der Lehrstuhlbibliothek erkläre ich mich einverstanden.

Garching bei München, den 17. Februar 2021 _____ (Tobias Egle)

Chair of Automatic Control (Prof. Dr.-Ing. habil. Boris Lohmann)
Technical University of Munich
Boltzmannstraße 15
85748 Garching bei München
Germany

Lehrstuhl für Regelungstechnik (Prof. Dr.-Ing. habil. Boris Lohmann)
Technische Universität München
Boltzmannstraße 15
85748 Garching bei München
Deutschland

Abstract

Previous research on friction estimation in robotic joints has been primarily focused on the dominant contribution of the drive unit friction originating in particular from the harmonic drive gear. With torque sensors mounted on the joint output side, the frictional effects of the drive units can be compensated by the torque controller to a large extend. However, in an assembled robot the friction in mechanical parts on the output side of the torque sensor still affects the actuation performance and leads to permanent control errors. This work aims at developing a whole-body friction estimation method that relies solely on internal position measurements of the robot and can capture the friction state on the output side of the joint torque sensor. Therefore, by comparison of a model-based acceleration estimate with the measured joint acceleration, obtained by numerical differentiation of the joint positions, a joint friction estimate can be determined. A simulation model is designed to evaluate the proposed method. Simulation results confirm that reliable friction torque estimates can be obtained given a sufficiently accurate dynamic model of the robot. It is shown that real-world imperfection like sensor noise, vibrations induced by the closed-loop control and inertia modeling errors limit the performance of the friction estimation in the experiment.

Kurzfassung

Bisherigere Forschung zur Reibungsschätzung in Robotergelenken hat sich hauptsächlich auf den dominanten Beitrag der Reibung in der Antriebseinheit konzentriert, die insbesondere vom Harmonic Drive Getriebe ausgeht. Mit auf der Abtriebseite des Gelenks montieren Drehmomentsensoren können die Reibungseffekte der Antriebseinheiten durch Regelung zu einem großen Teil kompensiert werden. In dem vollständig montierten Roboter führt die Reibung der mechanischen Bauteile auf der Abtriebsseite des Drehmomentsensors jedoch immer noch zu Abweichungen vom gewünschten Regelverhalten. Diese Arbeit zielt darauf ab, eine Methode zur Schätzung der Ganzkörperreibung zu entwickeln, die ausschließlich interne Messungen der Gelenkposition benötigt und die nicht ausgeregelte Reibung erfassen kann. Durch Vergleich einer modellbasierten Beschleunigungsschätzung mit der gemessenen Gelenkbeschleunigung, die durch numerische Ableitung der Gelenkpositionen bestimmt wird, kann somit eine Schätzung der Gelenkreibung ermittelt werden. Die vorgeschlagene Methode wird mittels eines Simulationsmodells evaluiert. Die Simulationsergebnisse bestätigen, dass bei einem ausreichend genauen dynamischen Modell des Roboters zuverlässige Schätzungen des Reibungsmoments ermittelt werden können. Es wird gezeigt, dass reale Beeinträchtigungen wie Sensorrauschen, durch die Regelung hervorgerufene Vibrationen und Modellierungsfehler der Trägheit des Roboters die Qualität der Reibungsschätzung im Experiment einschränken.

Contents

Chapter 1

Introduction

Legged locomotion is among the most fascinating research topics in robotics and continues to gain growing public attention. Videos of walking robots reach millions of people without difficulty with supporters envisioning the next breakthrough in the close future. At the same time is, what seems natural for humans, regarded as a very difficult problem for robots. Even with great progress in recent years, today's robots just barely reach a fraction of human locomotion capabilities. Many challenges regarding mechanical design, actuator performance and control theory remain to be solved.

Often, improvements are in particular limited by transferring walking performance achieved in simulation to real robots. Imperfections of the robot hardware like sensor noise, communication delays, inertia modeling errors and unmodeled joint friction impede real-world dynamic walking performance. These problems can be overcome to some extend by developing precise models of the robot and reducing noise and vibration levels as effectively as possible [6], although some problems remain.

Especially friction can only be modeled insufficiently due to the high complexity of interactions between two surfaces sliding against each other. Robots equipped with joint torque sensors, like the one discussed in this work, have the distinct benefit that the joint torque can be precisely controlled by the closed-loop torque control. Therefore, the main contribution to the joint friction originating from the motor and in particular the harmonic drive gear is for the most part compensated by the joint torque controller. However, friction in other mechanical parts on the output side of the torque sensor cannot be counteracted and leads to permanent control errors.

1.1 Task description

It is desirable to estimate the entire joint friction without additional sensors. Assuming that the internal drive unit friction is largely compensated by the torque controller, the joint friction consists dominantly of friction in mechanical parts on the output side of the torque sensor. This work aims to develop a whole-body friction torque estimation method that relies exclusively on the measurements supplied by internal sensors of the humanoid robot.

1.2 Content outline

The work is organized as follows. Chapter 2 summarizes related work of friction estimation and compensation in the field of robotics. In Chapter 3 an overview of different friction models is presented. Chapter 4 introduces the humanoid robot TORO and the dynamic model for walking robots. The whole-body joint friction estimation framework is derived in Chapter 5. Subsequently, the friction estimation is evaluated in simulation in Chapter 6. Different filter designs are presented in Chapter 7 to reduce noise and vibration of the experimental data and the friction estimation based on walking experiments is examined. Chapter 8 concludes the work.

Chapter 2

Related Work

Due to the abundance of physical phenomena that cause friction, model-based friction estimation of all kinds strongly relies on preceding measurements of the frictional torque in a robotic joint. Although some methods can directly estimate the friction model parameters based on the inverse dynamic model of the robot, they likewise depend on accurate measurements of the robot's state, internal torques and external forces/moments. In the following, an overview of different friction estimation approaches is presented.

2.1 Test-bed based joint friction estimation

The most straightforward method of determining the friction torque is to use a test-bed setup with a single joint. Torque sensors can supply precise measurements of the friction torque in desired parts of the assembly. The friction of different components like the motor and the harmonic drive gear can be considered separately. Consequently, accurate static and dynamic friction models with viscous, thermal and load dependencies have been developed [2, 13, 18]. These models are highly effective at modeling and compensating friction in the test-bed setup. They can also be used to model the friction of the investigated components in an assembled robot. However, the fixed friction parameters may change due to assembly precision, lubrication condition and wear of the mechanical parts. Furthermore, it is not always possible to analyze each joint separately in which case the friction estimation must be performed on the assembled robot.

2.2 Whole-body friction estimation with end-effector torque sensors

Most traditional humanoid robots are not equipped with joints torque sensors. They rely on accurate dynamic models of the robot and its environment in combination with a high-gain joint position control [5]. Hashlamon and Erbatur [10] use measured ground reaction forces in combination with a reduced dynamical model to estimate the joint torque. The friction is calculated as the difference of the supplied torque and the estimated joint torque. The method is based on the measurement approach when the leg is on the ground and a model-based friction estimation when the leg is in the swing phase. The parameters of the friction model are updated adaptively when the foot is in contact.

2.3 Multibody friction estimation and compensation with joint torque sensors

A friction observer based on joint torque measurements is presented in [12]. Similar to the momentum-based collision detection algorithms developed in [4], which observes external disturbance torques, this approach aims to identify the friction torque on the motor-side. It is shown that the observer produces an estimated friction torque which is equal to the low-pass filtered actual friction. Further, using the estimated torque for friction compensation, it is proven that the observer together with a passivity-based controller preserves the global asymptotic stability of the system and increases the accuracy of the robot.

2.4 Direct multibody parameter estimation

This method differs from the aforementioned models by directly determining the dynamic parameters of robots like inertia and friction using a least-squares optimization [8, 9]. The key idea is that the inverse dynamics are linear in the minimum parameters. These so-called base or lumped parameters are defined to be the minimum number of parameters from which the inverse dynamic model can be computed. By sampling the inverse dynamic equations while the robot is following a specific trajectory, an over-determined linear system can be constructed. The least-squares solution of the system of equations is found by the use of the pseudo-inverse. This model is dependent on joint acceleration, which is determined by numerical differentiation. It is therefore sensitive to noise and vibrations in the joint velocity. Moreover, the identification method requires parametrically exciting trajectories, such that the least-squares problem is well conditioned. In the case of friction estimation, it means that the robot needs to move through a large enough velocity range to get an accurate estimate of all friction phenomena.

2.5 Problem definition

Joint friction estimation is studied intensively for actuator components that have a major contribution to the friction in a robotic joint, i.e. the motor and the harmonic drive gear. Especially for joints with a high transmission ratio, a well identified and modeled friction behavior helps to significantly improve the position tracking accuracy. The friction of the drive units can be determined separately. Even if the model is not ideal, in torque-controlled robots with link-side joint torque sensors, a sufficiently fast control approach in combination with the friction compensation can keep the torque error to a minimum. However, motor and harmonic drive gear are not the only contributors to the joint friction. There are bearings and for some joints motion transmission mechanisms on the output side of the torque sensor for which the friction behavior cannot be determined or controlled. Furthermore, there might be torque offsets resulting from the calibration routine. This work aims at developing an estimation model that can observe the friction torque and torque offsets in a fully assembled robot.

Chapter 3

Friction Models

Friction is present in all mechanical parts that are in contact and opposes their motion. It plays an important role in the design of many control systems as it can lead to unwanted deviation from the desired control quality. Friction can cause permanent control errors, stick-slip motion or limit cycles if neglected. Especially for robotic systems with strongly varying velocities, high-precision positioning tasks and many velocity reversals, a well identified friction model can significantly improve the actuation performance. There exist many different approaches to friction modeling, which can generally be divided into two categories: static and dynamic friction models.

3.1 Static friction models

Static friction models describe the friction torque τ_f as a static function of velocity. In past centuries models of different complexity have been developed that each describes certain components of the frictional behavior.

The earliest model describes a friction torque that opposes the motion of two bodies relative to each other and is independent of velocity. It is known as Coulomb friction and given by:

$$\tau_f = \tau_c \operatorname{sgn}(\dot{q}), \tag{3.1}$$

where the parameter τ_c specifies the magnitude of the piecewise constant Coulomb friction. The friction torque at zero velocity is not defined which results in a discontinuity at rest.

The viscous friction describes the velocity-strengthening part of the friction torque. It originates from the viscosity of lubricants that resist the motion of solid bodies in contact with the fluid or between adjacent layers of the fluid itself. In its simplest representation the friction torque is given as a linear function of velocity:

$$\tau_f = \tau_v \dot{q}, \tag{3.2}$$

with τ_v defining the slope of the viscous friction.

The Stribeck friction accounts for the phenomenon that the friction torque close to the standstill has a negative derivative with respect to the velocity. At rest, it is higher than the Coulomb friction and decreases continuously from the static friction level. The

Stribeck effect is also called the velocity-weakening part of the frictional behavior. It is most commonly modeled by an exponential function:

$$\tau_f = \operatorname{sgn}(\dot{q}) \left(\tau_c + (\tau_s - \tau_c) e^{-|\dot{q}/v_s|^{\delta_s}} \right). \tag{3.3}$$

Here τ_s is the static friction torque, v_s the Stribeck velocity and δ_s the exponent parameter of the Stribeck non-linearity. Different vales for δ_s are suggested in [14], in this work the Gaussian parametrization with $\delta_s = 2$ is selected [1, 18].

3.2 Dynamic friction models

The static friction models describe friction as a function of steady velocities. However, experiments exhibit frictional effects that cannot be represented by static models. This includes phenomena like microslip or presliding displacement, hysteretic behavior and varying breakaway torque. These effects can be captured by dynamic friction models which use additional states to describe the friction torque in terms of differential equations. A well known dynamic friction model in robotics is the LuGre model [3]. Dynamic models are employed when the friction torque is accurately measurable and there is a need for precision beyond the capabilities of the static models [7, 13, 18]. For this work, however, the determination of the friction torque itself is afflicted with uncertainty, such that the static friction models are entirely sufficient and the dynamic models are merely mentioned for completeness.

3.3 Friction models in simulation

All static friction models described above, except pure viscous friction, are discontinuous at the origin due to the use of the signum function $\operatorname{sgn}(x)$ to determine the direction of the friction torque. A simulated friction model that incorporates more than the velocity-strengthening effect of the viscous friction has to deal with the computational challenges presented by this discontinuity. Very small time steps are required to accurately determine the sign change of the velocity. When the simulation rate cannot be adjusted and very small time steps are infeasible, a different approach is needed to avoid oscillations due to rapidly changing friction torques in the vicinity of the discontinuity. It is suggested to weaken the discontinuity and define a continuous model as

$$\tau_f = \tau_v \dot{q} + \tanh(a\dot{q}) \left(\tau_c + (\tau_s - \tau_c) e^{-|\dot{q}/v_s|^{\delta_s}} \right) + \tau_{os}, \tag{3.4}$$

with the coefficient a specifying the slope of the hyperbolic tangent function. The parameter τ_{os} considers an offset torque which may originate from calibration errors.

The friction model is further simplified by defining $\tau_s = (1 + S)\tau_c$, where the parameter S determines the relative size of the Stribeck curve:

$$\tau_f = \tau_v \dot{q} + \tau_c \tanh(a\dot{q}) \left(1 + S e^{-|\dot{q}/v_s|^{\delta_s}} \right) + \tau_{os}. \tag{3.5}$$

The presented model is selected to cover the relevant friction phenomena expected in the robotic joint. It is a combination of the aforementioned static models combining Coulomb, viscous and Stribeck friction and contains the additional torque offset term. The choice of a friction model in simulation is arbitrary, however, the specific model aims at good comparability of the simulation and experimental results in Chapter 6 and Chapter 7, respectively.

Chapter 4

The Humanoid Robot TORO

In the following, a brief introduction of the mechanical design and dynamic model of the torque-controlled humanoid robot TORO is presented.

4.1 Overview of TORO's mechanical design

Being able to roughly manipulate the same workspace as humans and use the same principles of locomotion, TORO has a much human-like physique. Its total weight measures 79.2 kg with a height of 174 cm. The robot has 25 torque-controlled revolute joints, 6 in each limb, and one additional joint in the waist. The 2 revolute joints in the neck are position-controlled. An overview of the fundamental dimensions and joint configuration is given in Fig. 4.1. The joints were built with drive units and electronics from the KUKA-LWR[1] arm. They consist of a RoboDrive brushless DC motor with safety break and incremental motor position sensor, a Harmonic Drive gear unit, a torque sensor and an absolute output position sensor. The motor type and gear ratio vary between joints depending on the torque requirement. The particular specification for each joint is given in Table 4.1.

Relevant for the friction estimation are mechanisms that are placed on the output side of the torque sensor, like the parallel bar mechanism in TORO's ankles. To decrease the shank's inertia and realize a slim ankle design, the ankle pitch motor (F) is located close to the knee. The friction and backlash caused by this mechanism, like that of all other mechanical parts and bearings mounted on the output side of the torque sensor, are not measurable by any of TORO's sensors.

4.2 Floating base model

This Section gives a brief overview of the floating base model for legged robots. Starting from the dynamic model of a stationary robot, the constraint equation of motion of a robot with a floating base is derived.

[1] A lightweight robot (LWR) originally developed at DLR for which the *KUKA Roboter GmbH* acquired licensing in 2004.

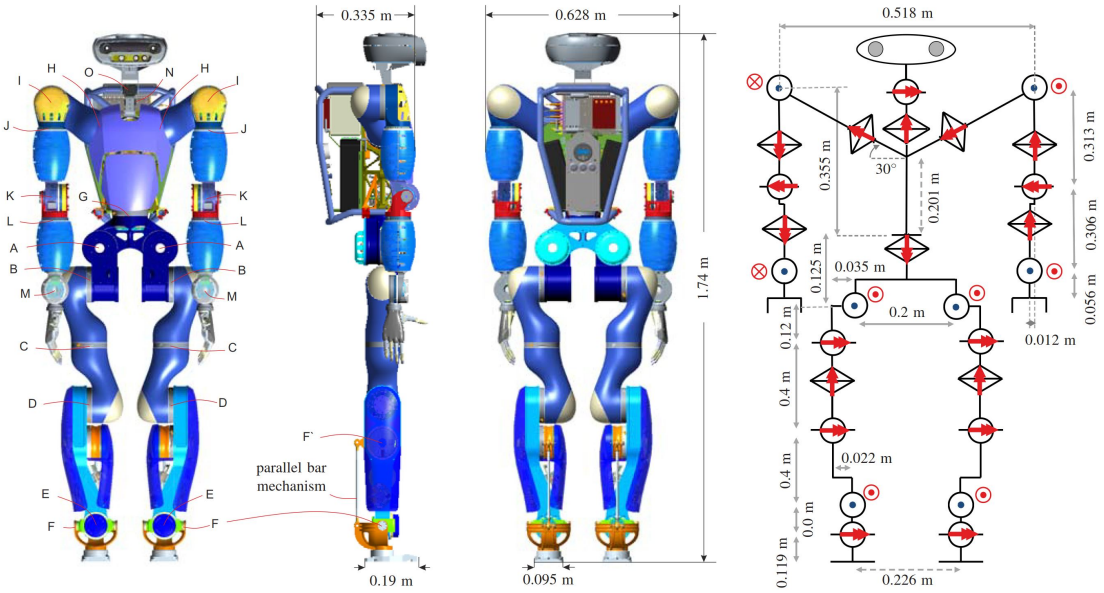

Figure 4.1: Overview of TORO's dimensions and joint configuration [6]

Table 4.1: Overview of TORO's joint specification [6]

joint	**motor**	**gear ratio**	$\dot{q}_{max}$	τ_{max}	**range** [°]
A - hip roll	ILM85	160	110 °/s	176 Nm	±45..±90
B - hip pitch	ILM70	160	157 °/s	100 Nm	-115 .. 90
C - hip yaw	ILM70	160	157 °/s	100 Nm	±120
D - knee	ILM85	100	176 °/s	130 Nm	±105
E - ankle roll	ILM50	160	120 °/s	40 Nm	±19.5
F - ankle pitch	ILM85	100	176 °/s	130 Nm	±45
G - waist	ILM70	160	157 °/s	100 Nm	±120
H - shoulder 1	ILM70	160	157 °/s	100 Nm	±120
I - shoulder 2	ILM70	160	157 °/s	100 Nm	-15..180
J - shoulder 3	ILM50	160	120 °/s	40 Nm	±105
K - elbow	ILM50	160	120 °/s	40 Nm	0..148
L - wrist 1	ILM50	160	120 °/s	40 Nm	-145..118
M - wrist 2	ILM50	160	120 °/s	40 Nm	±105
N - neck yaw	MS106T	225	270 °/s	8.4 Nm	±90
O - neck pitch	MS106T	225	270 °/s	8.4 Nm	-30..90

4.2.1 Dynamic model: From fixed base to floating base

As indicated by the name, robots with a floating base differ from their stationary companions known from factory floors by the ability to freely move around. In the case of legged robots, they are able to walk on two or more legs. Most industrial robots are attached to the ground and actuated in every degree of freedom. The equations of motion for these fully actuated robots can be written as

$$\mathbf{M}(\mathbf{q})\ddot{\mathbf{q}} + \mathbf{h}(\mathbf{q}, \dot{\mathbf{q}}) = \boldsymbol{\tau} + \boldsymbol{\tau}_{ext}. \tag{4.1}$$

Here $\mathbf{M}$ is the inertia matrix, $\mathbf{h}$ contains Coriolis and centrifugal forces, as well as gravity and friction forces. The vectors $\boldsymbol{\tau}$ and $\boldsymbol{\tau}_{\mathbf{ext}}$ are the joint and external forces/torques, respectively. It is assumed that every force that is applied on the robot or exerted by the robot itself is counteracted by the rigid connection to the ground.

By detaching the robot from the environment, it can now freely move around and thus gains an additional six degrees of freedom. To account for these, the state of the free floating base is added to the robot's configuration. It is described by the position $\mathbf{x}_{base} \in \mathbb{R}^3$ and orientation $\mathbf{R}_{base} \in SO(3)$ of the body frame relative to the world frame. The hip functions as the base link to which the body frame is attached. In the base state vector $\mathbf{q}_{base} \in \mathbb{R}^6$ the orientation is represented in local coordinates $\boldsymbol{\alpha}_{base} \in \mathbb{R}^3$, e.g. roll-pitch-yaw angles. Combined with the joint position $\mathbf{q}_{jnt} \in \mathbb{R}^n$ the variables are concentrated into a single state vector:

$$\mathbf{q} = \begin{bmatrix} \mathbf{x}_{base} \\ \boldsymbol{\alpha}_{base} \\ \mathbf{q}_{jnt} \end{bmatrix} = \begin{bmatrix} \mathbf{q}_{base} \\ \mathbf{q}_{jnt} \end{bmatrix} \in \mathbb{R}^{6+n}. \tag{4.2}$$

With the base no longer connected to the ground, the absorption of reaction forces by the environment is lost. For every contact the robot makes with its environment, there is an equal and opposite force acting on the robot itself. For simplicity, it is assumed that all external forces act at the end-effector frames. Then $\boldsymbol{\tau}_{ext}$ simplifies to

$$\boldsymbol{\tau}_{ext} = \mathbf{J}(\mathbf{q})^T \mathbf{W}, \tag{4.3}$$

where $\mathbf{J} \in \mathbb{R}^{m \times n}$ is the Jacobi matrix[2] and $\mathbf{W} \in \mathbb{R}^m$ is the Cartesian wrench, a six-dimensional vector of external Cartesian forces and torques.

The additional six degrees of freedom of the base cannot be controlled directly. Thus, the robots with a floating base belong to a class called underactuated systems, for which the equation of motion is given by

$$\mathbf{M}(\mathbf{q})\ddot{\mathbf{q}} + \mathbf{h}(\mathbf{q}, \dot{\mathbf{q}}) = \mathbf{S}^T\boldsymbol{\tau} + \mathbf{J}^T\mathbf{W}. \tag{4.4}$$

The matrix $\mathbf{S} = [\mathbf{0}_{n\times 6}\ \mathbf{I}_{n\times n}]$ is a selection Matrix, that selects only the bottom n components of $\boldsymbol{\tau}$, which can be actuated directly.

[2]Supposing the forward kinematics $\mathbf{x} = \varphi(\mathbf{q})$ is a local mapping between the configuration space $\mathbf{q} \in \mathbb{R}^n$ and an m-dimensional task space $\mathbf{x} \in \mathbb{R}^m$. Then the velocity transformation between these spaces is given by: $\dot{\mathbf{x}} = \frac{d\varphi(\mathbf{q})}{dt} = \frac{\partial\varphi(\mathbf{q})}{\partial\mathbf{q}}\dot{\mathbf{q}} = \mathbf{J}(\mathbf{q})\dot{\mathbf{q}}$, where $\mathbf{J}(\mathbf{q})$ is the Jacobi Matrix. Considering that power is independent of representation, it can be shown that: $P_x = \dot{\mathbf{x}}^T\mathbf{W} = \dot{\mathbf{q}}^T\mathbf{J}^T\mathbf{W} = \dot{\mathbf{q}}^T\boldsymbol{\tau} = P_q$ and thus $\boldsymbol{\tau} = \mathbf{J}^T\mathbf{W}$.

4.2.2 Contact constraints on the robot

As the robot is not floating in space, it needs to make contact with its environment. For walking, it is assumed that the feet are in contact with the ground without slipping. More precisely, the task space position of the foot in contact is constant in the contact phase. This leads to a constraint on the task space velocities: $\dot{\mathbf{x}} = \mathbf{J}\dot{\mathbf{q}} = \mathbf{0}$. Since the equation of motion relates torques and external forces to accelerations, another time derivative of the constraint is needed. It yields: $\ddot{\mathbf{x}} = \mathbf{J}\ddot{\mathbf{q}} + \dot{\mathbf{J}}\dot{\mathbf{q}} = \mathbf{0}$.

The constraint equation of motion is given by:

$$\begin{aligned} &\mathbf{M}(\mathbf{q})\ddot{\mathbf{q}} + \mathbf{h}(\mathbf{q}, \dot{\mathbf{q}}) = \mathbf{S}^T\boldsymbol{\tau} + \mathbf{J}^T\mathbf{W} \\ &\mathbf{J}\ddot{\mathbf{q}} = -\dot{\mathbf{J}}\dot{\mathbf{q}}. \end{aligned} \tag{4.5}$$

It consists of $6 + n + m$ equations in as many unknowns and fully describes the underactuated robot in contact with its environment.

Chapter 5

Whole-body Joint Friction Estimation

In this Chapter the friction torque estimation based on the constraint dynamic equations of the robot is derived.

5.1 General method

The joint friction torque on the output side of the torque sensor is not directly measurable, therefore it needs to be estimated through a quantity that depends upon the desired variable. As described in Chapter 4 the equation of motion of the robot relates torques and external forces to accelerations. The vector $\mathbf{h}$ in (4.5) can be explicitly written as

$$\mathbf{h} = \mathbf{C}\dot{\mathbf{q}} + \boldsymbol{\tau}_g - \mathbf{S}^T\boldsymbol{\tau}_{fric}, \tag{5.1}$$

with $\mathbf{C}$ being the Coriolis and centrifugal matrix, $\boldsymbol{\tau}_g$ the vector of gravitational forces and torques and $\boldsymbol{\tau}_{fric}$ the joint friction torques. Inserting (5.1) in the constraint equation of motion (4.5) yields:

$$\begin{aligned} &\mathbf{M}\ddot{\mathbf{q}} + \mathbf{C}\dot{\mathbf{q}} + \boldsymbol{\tau}_g = \mathbf{S}^T(\boldsymbol{\tau}_j + \boldsymbol{\tau}_{fric}) + \mathbf{J}^T\mathbf{W} \\ &\mathbf{J}\ddot{\mathbf{q}} = -\dot{\mathbf{J}}\dot{\mathbf{q}}. \end{aligned} \tag{5.2}$$

Therefore, the acceleration $\ddot{\mathbf{q}}$ is directly dependent on the joint friction torque $\boldsymbol{\tau}_{fric}$. In order to determine $\boldsymbol{\tau}_{fric}$, an estimate of the acceleration without the unknown friction torque is calculated and compared to the measured acceleration, obtained by numerical differentiation of the robots state $\mathbf{q}$. Assuming a sufficiently accurate dynamic model, the resulting difference in acceleration originates from the joint friction torque.

5.2 Solving constraint dynamics to estimate accelerations

In the following derivation, the equation (5.2) is concertized for the humanoid robot TORO with its 27 joints, resulting together with the 6 base coordinates in a system of $33 + m$ equations. The friction estimation is performed for the 25 torque-controlled

joints. The 2 position-controlled joints in the neck need to be considered separately. In the torque-control approach, there is no torque supplied for these joints. However, a non-zero torque is required to keep the head in the desired position. In the friction estimation, it is assumed that there is no relative motion between the head and the upper body. Therefore, the additional constraint $\ddot{\mathbf{q}}_{pc} = \mathbf{0}$ is applied to the robot's dynamic equations in the following way. The selection matrices

$$\mathbf{S}_{tc} = \begin{bmatrix} \mathbf{0}_{25\times 6} & \mathbf{I}_{25\times 25} & \mathbf{0}_{25\times 2} \end{bmatrix} \quad \text{and} \quad \mathbf{S}_{pc} = \begin{bmatrix} \mathbf{0}_{2\times 31} & \mathbf{I}_{2\times 2} \end{bmatrix} \tag{5.3}$$

are used to separate the torque and position-controlled joint torques $\boldsymbol{\tau}_{tc} \in \mathbb{R}^{25}$ and $\boldsymbol{\tau}_{pc} \in \mathbb{R}^2$, respectively. The friction torque is also divided into two categories. Here, only the friction torque $\boldsymbol{\tau}_{fric,tc} \in \mathbb{R}^{25}$ for the torque-controlled joints exists, for which the friction estimation is performed. As the friction of the position-controlled joints cannot be estimated, the friction torque $\boldsymbol{\tau}_{fric,pc} \in \mathbb{R}^2$ is assumed to be zero. To improve readability, the friction torque of the torque-controlled joints $\boldsymbol{\tau}_{fric,tc}$ is denoted $\boldsymbol{\tau}_f$ for the remainder of this work. Combined with the task space constraints in (5.2) the full constraint equation of motion is given by:

$$\mathbf{M}\ddot{\mathbf{q}} + \mathbf{C}\dot{\mathbf{q}} + \boldsymbol{\tau}_g = \mathbf{S}_{tc}^T(\boldsymbol{\tau}_{tc} + \boldsymbol{\tau}_f) + \mathbf{S}_{pc}^T\boldsymbol{\tau}_{pc} + \mathbf{J}^T\mathbf{W} \tag{5.4a}$$

$$\mathbf{J}\ddot{\mathbf{q}} = -\dot{\mathbf{J}}\dot{\mathbf{q}} \tag{5.4b}$$

$$\mathbf{S}_{pc}\ddot{\mathbf{q}} = \mathbf{0}. \tag{5.4c}$$

In the following derivation, the unknown friction term $\mathbf{S}_{tc}^T\boldsymbol{\tau}_f$ is neglected to obtain the reference acceleration estimate without frictional effects. Both constraints (5.4b) and (5.4c) are linear equality constraints of the form $\mathbf{J}_c(\mathbf{q})\ddot{\mathbf{q}} = \mathbf{b}(\mathbf{q}, \dot{\mathbf{q}})$ and can therefore be combined to a single constraint:

$$\mathbf{M}\ddot{\mathbf{q}} + \mathbf{C}\dot{\mathbf{q}} + \boldsymbol{\tau}_g = \mathbf{S}_{tc}^T\boldsymbol{\tau}_{tc} + \mathbf{J}_c^T\boldsymbol{\lambda} \tag{5.5a}$$

$$\mathbf{J}_c\ddot{\mathbf{q}} = \mathbf{b} \tag{5.5b}$$

with

$$\mathbf{J}_c = \begin{bmatrix} \mathbf{J} \\ \mathbf{S}_{pc} \end{bmatrix} \quad \text{and} \quad \mathbf{b} = \begin{bmatrix} -\dot{\mathbf{J}} \\ \mathbf{0} \end{bmatrix} \dot{\mathbf{q}} \quad \text{and} \quad \boldsymbol{\lambda} = \begin{bmatrix} \mathbf{W} \\ \boldsymbol{\tau}_{pc} \end{bmatrix}. \tag{5.6}$$

The vector of constraint forces and torques $\boldsymbol{\lambda} \in \mathbb{R}^{(m+2)}$ can be interpreted as a set of Lagrange multipliers. With the constraint equations, the resulting system consists of $33 + m + 2$ equations in as many unknowns. The goal is to reduce the constraint system to its original 33 equations in 33 unknowns. It is achieved by first determining the vector of Lagrange multipliers using the constraint equation. With $\mathbf{M}$ being symmetric positive definite and therefore invertible, equation (5.5a) can be solved for

$$\ddot{\mathbf{q}} = \mathbf{M}^{-1}\left(\mathbf{S}_{tc}^T\boldsymbol{\tau}_{tc} + \mathbf{J}_c^T\boldsymbol{\lambda} - \mathbf{C}\dot{\mathbf{q}} - \boldsymbol{\tau}_g\right) \tag{5.7}$$

and inserted in the constraint equation (5.5b):

$$\begin{aligned} &\mathbf{J}_c\mathbf{M}^{-1}\left(\mathbf{S}_{tc}^T\boldsymbol{\tau}_{tc} + \mathbf{J}_c^T\boldsymbol{\lambda} - \mathbf{C}\dot{\mathbf{q}} - \boldsymbol{\tau}_g\right) = \mathbf{b} \\ &\Rightarrow \underbrace{\mathbf{J}_c\mathbf{M}^{-1}\mathbf{J}_c^T}_{\mathbf{A}}\boldsymbol{\lambda} = \mathbf{b} + \mathbf{J}_c\mathbf{M}^{-1}\left(\mathbf{C}\dot{\mathbf{q}} + \boldsymbol{\tau}_g - \mathbf{S}_{tc}^T\boldsymbol{\tau}_{tc}\right). \end{aligned} \tag{5.8}$$

In order to solve for the generalized vector $\boldsymbol{\lambda}$, matrix $\mathbf{A}$ needs to be invertible. Like $\mathbf{M}$, $\mathbf{M}^{-1}$ is also symmetric positive definite. The selection matrix $\mathbf{S}_{pc}$ only adds two independent columns to $\mathbf{J}_c$. Hence, the invertibility of $\mathbf{A}$ depends on $\mathbf{J}$. In general, the matrix $\mathbf{J}\mathbf{M}^{-1}\mathbf{J}^T \in \mathbb{R}^{m\times m}$ is invertible if the task space dimension m is equal or lower dimensional than the dimension of the configuration space n and $\mathbf{J}$ has at least rank m. Then $\mathbf{A} \in \mathbb{R}^{(m+2)\times(m+2)}$ is invertible and $\boldsymbol{\lambda}$ can be written as

$$\boldsymbol{\lambda} = \left(\mathbf{J}_c\mathbf{M}^{-1}\mathbf{J}_c^T\right)^{-1}\left(\mathbf{b} + \mathbf{J}_c\mathbf{M}^{-1}\left(\mathbf{C}\dot{\mathbf{q}} + \boldsymbol{\tau}_g - \mathbf{S}_{tc}^T\boldsymbol{\tau}_{tc}\right)\right). \tag{5.9}$$

Now the constraint forces and torques are expressed by only known quantities. Inserting equation (5.9) back into (5.5a) and solving for $\ddot{\mathbf{q}}$ gives an estimate of the accelerations:

$$\begin{aligned}\ddot{\mathbf{q}}_{est} = \mathbf{M}^{-1}\ & \mathbf{J}_c^T\left(\mathbf{J}_c\mathbf{M}^{-1}\mathbf{J}_c^T\right)^{-1}\mathbf{b} \\ & + \mathbf{M}^{-1}\underbrace{\left(\mathbf{I} - \mathbf{J}_c^T\left(\mathbf{J}_c\mathbf{M}^{-1}\mathbf{J}_c^T\right)^{-1}\mathbf{J}_c\mathbf{M}^{-1}\right)}_{\mathbf{N}}\mathbf{S}_{tc}^T\boldsymbol{\tau}_{tc} \\ & + \mathbf{M}^{-1}\underbrace{\left(\mathbf{J}_c^T\left(\mathbf{J}_c\mathbf{M}^{-1}\mathbf{J}_c^T\right)^{-1}\mathbf{J}_c\mathbf{M}^{-1} - \mathbf{I}\right)}_{-\mathbf{N}}\left(\mathbf{C}\dot{\mathbf{q}} + \boldsymbol{\tau}_g\right).\end{aligned} \tag{5.10}$$

Matrix $\mathbf{N}$ is the null space projection matrix which ensures that the constraints on contact/foot and joint space accelerations are satisfied by removing the generalized torque components that act on the constraints.

5.3 Joint friction torque estimation

The vector of measured accelerations $\ddot{\mathbf{q}}_{msr}$ is obtained by numerical differentiation and includes the in (5.4a) stated friction term $\mathbf{S}_{tc}^T\boldsymbol{\tau}_f$. A friction estimate can be calculated through the difference of the measured acceleration and the estimated acceleration:

$$\Delta\ddot{\mathbf{q}} = \ddot{\mathbf{q}}_{msr} - \ddot{\mathbf{q}}_{est} = \mathbf{M}^{-1}\mathbf{N}\ \mathbf{S}_{tc}^T\boldsymbol{\tau}_f. \tag{5.11}$$

In the following, the friction torque estimation is discussed for different support conditions. The null space projection matrix $\mathbf{N}$ has rank $33-(m+2)$. In the single support phase, due to the constraint (5.4b), one foot of the robot is fixed to the ground. In this case, the constraint space dimension m equals 6, lowering the rank of matrix $\mathbf{N}$ to 25. As a result of the free floating base, there are still enough degrees of freedom to move each joint individually and a tree structure similar to classical fixed-based robots is obtained. The robot is balancing on one leg and the base frame located at the hip can be considered as the task space. The equal dimension of the leg's configuration space n_{leg} and base frame space $dim(\mathbf{q}_{base})$ suggests, apart from singularities, a unique mapping between the configuration space and the base frame task space: $n_{leg} = dim(\mathbf{q}_{base}) = 6$. As a consequence, a given joint acceleration difference should yield a unique friction torque. However, Matrix $\mathbf{M}^{-1}\mathbf{N}$ is of reduced rank. The rank deficiency can readily be resolved by selecting only the equations of the 25 torque-controlled joints for which $\boldsymbol{\tau}_f$ exists. The remaining system of equations is given by:

$$\Delta\ddot{\mathbf{q}}_{tc} = \mathbf{S}_{tc}^T\ddot{\mathbf{q}}_{msr} - \mathbf{S}_{tc}^T\ddot{\mathbf{q}}_{est} = \underbrace{\mathbf{S}_{tc}\mathbf{M}^{-1}\mathbf{N}\mathbf{S}_{tc}^T}_{\mathbf{M}_{mod}^{-1}}\boldsymbol{\tau}_f. \tag{5.12}$$

The inverse of $\mathbf{M}_{mod}^{-1}$ can be uniquely determined and an exact solution is found. The joint friction torque in the single support phase is given by:

$$\boldsymbol{\tau}_f = \underbrace{\left(\mathbf{S}_{tc}\mathbf{M}^{-1}\mathbf{E}\mathbf{S}_{tc}^T\right)^{-1}}_{\mathbf{M}_{mod}} \Delta\ddot{\mathbf{q}}_{tc}. \tag{5.13}$$

In the double support phase, both feet are on the ground and the constraint space dimension m equals 12. A closed-loop kinematic is obtained and the mapping from configuration space to base frame task space is under-determined. That means any feasible base frame task can be realized while additional degrees of freedom remain in the null space of the mapping. Thus, the same acceleration difference can be produced by multiple different friction torques. As a consequence, the matrix $\mathbf{M}_{mod}^{-1}$ becomes singular and the system of equations (5.13) has multiple solutions. A particular solution can be found using a pseudo-inverse but it is not exact. It finds the minimum norm solution to the system of equations. In the particular case, it yields the minimal friction to achieve a given acceleration difference, which is not the correct solution in most cases. Therefore, the friction torque cannot be accurately estimated in the double support phase.

Chapter 6

Simulation

Extending the existing simulation environment of the humanoid robot TORO, a friction model and estimation framework based on the method described in Chapter 5 is implemented in Matlab Simulink. There are two different simulators, one realized in Simulink and the other is part of an external software platform called OpenHRP (Open Architecture Human-centered Robotics Platform). Both are employed to evaluate the friction torque estimates based on the predefined friction model in Chapter 3.

6.1 Validation of friction torque estimation with Simulink simulation

The Simulink simulator solves the forward dynamics in a similar way as in Chapter 5 by constraining task space acceleration to compute external forces. A forward Euler integration method is used to compute velocities and positions. All other signals are returned without measurement noise and time delays. Therefore, this simulation is especially suitable to investigate the friction estimation under ideal conditions.

6.1.1 Friction estimation under different support conditions

As a first test, a friction torque based on the model in (3.5) is applied to a single joint. Because the knee joints have one of the largest velocity ranges, the target friction torque is added to the commanded torque of the right knee. Instead of obtaining $\ddot{\mathbf{q}}_{msr}$ by numerical differentiation, a ground truth acceleration is calculated in the same way as the estimated torque in (5.10), but with the additional friction. The friction estimate in the single support phase is determined with (5.13). As described in the previous Chapter the matrix $\mathbf{M}_{mod}^{-1}$ cannot be inverted in the double support phase due to the torque redundancy, as multiple combinations of joint friction torques can yield the same acceleration difference $\Delta\ddot{\mathbf{q}}_{tc}$. Thus the following optimization problem is constructed to resolve the redundancy:

$$\min_{\boldsymbol{\tau}_f} \frac{1}{2}(\Delta\ddot{\mathbf{q}}_{tc} - \mathbf{M}_{mod}^{-1}\boldsymbol{\tau}_f)^T\mathbf{W}(\Delta\ddot{\mathbf{q}}_{tc} - \mathbf{M}_{mod}^{-1}\boldsymbol{\tau}_f) + \frac{1}{2}\boldsymbol{\tau}_f^T\boldsymbol{\lambda}\boldsymbol{\tau}_f, \tag{6.1}$$

where $\boldsymbol{\lambda}$ and $\mathbf{W}$ are diagonal weighting matrices. The term $\frac{1}{2}\boldsymbol{\tau}_f^T\boldsymbol{\lambda}\boldsymbol{\tau}_f$ is added to the objective in order to penalize high torque values. The resulting friction torques for the single and double support phase are plotted in Fig. 6.1 for a total of 5 steps of the robot.

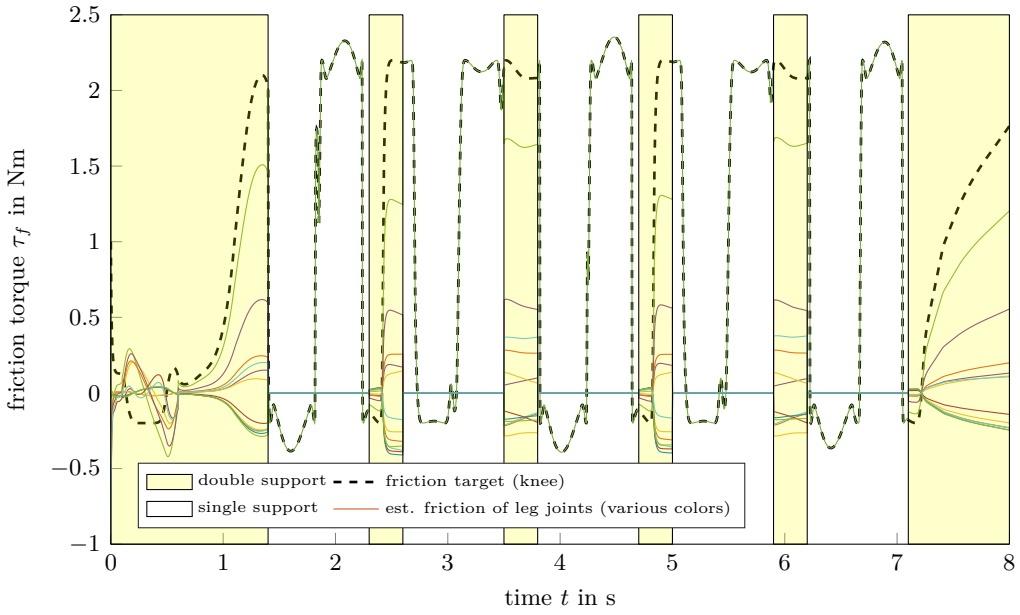

Figure 6.1: Friction torque estimation with target friction in the right knee

It can be observed that the estimated friction torque in the single support phase can be recovered exactly. The friction torque in the knee precisely follows the target friction and all other estimated torques are zero. In the double support phase, however, the plot displays various measures of friction resulting from the non-unique map between torques and accelerations as expected. Therefore, in the following observations, only the single support phase is selected for friction estimation.

6.1.2 Sensitivity towards phase delays

To get a more realistic estimation of the achievable real-world performance of the algorithm, the measured acceleration needs to be determined by numerical differentiation as no acceleration sensors are available. Two basic types of discrete time derivatives are considered here: central and backward finite differences [15]. The central difference

$$\dot{y}[t_n] = \frac{y[t_{n+1}] - y[t_{n-1}]}{2\Delta t} \tag{6.2}$$

gives a better approximation of the derivative at a discrete time t_n, but it relies on future data that is not available in a real-time system. The backward difference

$$\dot{y}[t_n] = \frac{y[t_n] - y[t_{n-1}]}{\Delta t} \tag{6.3}$$

is realizable in a real-time system. However, a causal discrete derivative in a real-time application is always accompanied by a phase shift. The sensitivity of the friction estimation with regard to the phase delay is investigated in Fig. 6.2. The friction torque is still applied to the right knee only. In the left support phase, that is when the right leg is

above the ground, the friction torque of the right knee can be recovered very accurately for all derivative schemes. Especially when plotted over joint velocity (Fig. 6.3), the tracking error can be observed clearly in the support phase of the right leg. Here, the small phase shift of the backward discrete derivative causes a notable deviation from the desired friction torque. It results from the fact that the supporting leg feels a much greater inertia than the swinging leg. The friction torque is given by $\boldsymbol{\tau}_f = \mathbf{M}_{mod}\Delta\ddot{\mathbf{q}}_{tc}$ (eq. (5.13)), in the support phase, a smaller difference in acceleration multiplied by a larger inertia must yield the same friction as in the swing phase of the leg. This results in a considerable sensitivity of the friction estimation in the support phase as for some joints there are up to three orders of magnitude difference in the diagonal elements of the mass matrix $\mathbf{M}_{mod}$ between the support and the aerial phase of the leg.

There is no feedback from the friction estimation to the robot control system, therefore all other input signals of the friction model can be delayed to correct for the phase shift of the backward discrete derivative. This leads to a more accurate friction approximation at the cost of decimating the real-time ability. Since the friction estimation is not designed to be real-time capable due to reasons discussed in Chapter 7, it can be readily tolerated. Hence, also the central derivative as an offline discrete differencing scheme leads to an increase in accuracy over the backward derivative. Its finite time step is twice as long as the time step of the backward derivative, though it still gives a better approximation of the joint acceleration. Nevertheless, this shows a considerable sensitivity of the method towards phase delays. For the further proceeding, especially with regards to filtering, it is important to prevent unidirectional distortions of the signal in the time domain.

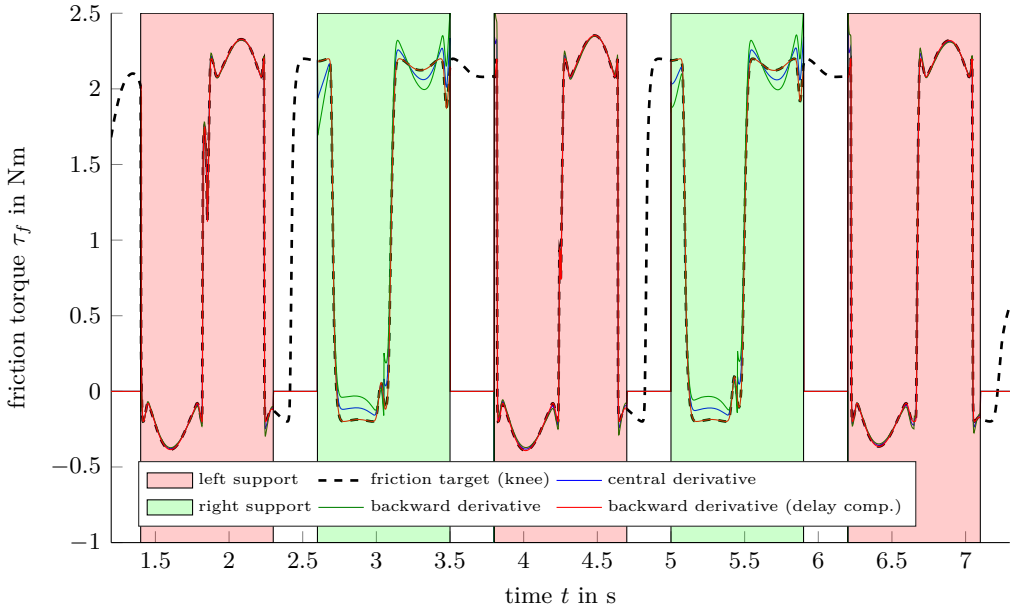

Figure 6.2: Comparison of discrete derivative schemes plotted over time

6.2 OpenHRP robot simulation environment

The next step towards experimental identification is using the OpenHRP simulation environment. It is a virtual humanoid robot platform consisting of a multibody simulator with contact and collision computation between arbitrary polyhedral objects [11].

6.2.1 Estimation sensitivity in more realistic simulation

The signals obtained from the OpenHRP interface are outputs from simulated sensors like gyroscope, force torque sensors, position encoders and joint torque sensors. Due to the more realistic and complex simulation approach, they are not as clean as the signals from the previous simulator but still without significant noise, except for the lift-off and touch-down interval of the feet. In these moments the contact constraints are instantaneously removed or enabled which leads to a sudden change in velocity if it is not close enough to zero already, and thereby high accelerations. Moreover, the added friction torque amplifies this effect because it hinders very slow velocities before the contact occurs. Therefore, the first 0.10 and the last 0.05 seconds of the single support phase are excluded from the friction estimation. As previously observed, Fig. 6.4 shows that the estimation method is overly sensitive in the stance phase and a small error in acceleration difference amplifies to a significant deviation in the estimated friction. However, the friction torque can still be obtained accurately using only the swing phase of the walking cycle as displayed in Fig. 6.5a. The friction torque is applied not only to the knee as before but to all leg joints in Fig. 6.5b. By comparison of the two figures, it can be confirmed, that there is no interference between the joints, and each joint friction can be distinguished from another.

6.2.2 Parameter identification

In order to determine the performance of the friction estimation, a non-linear least-squares optimization is performed to identify the parameters of the friction model and compare them to the previously defined target values. The parameters are chosen to

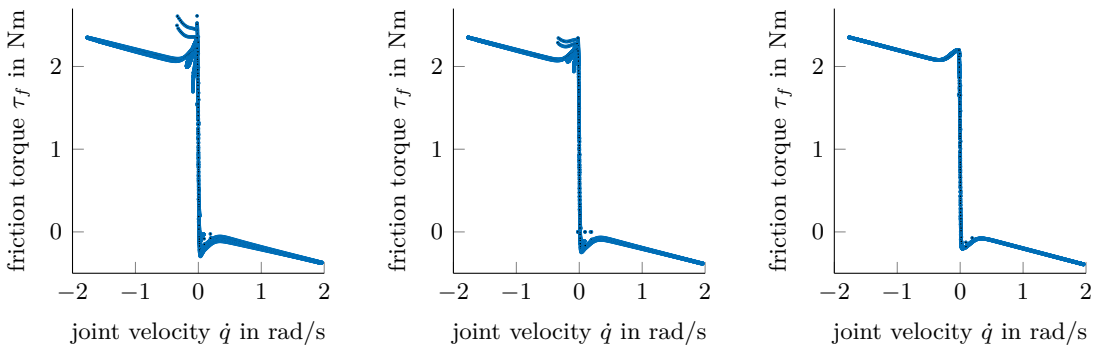

(a) backward (b) central (c) backward (delay comp.)

Figure 6.3: Comparison of discrete derivative schemes plotted over joint velocity

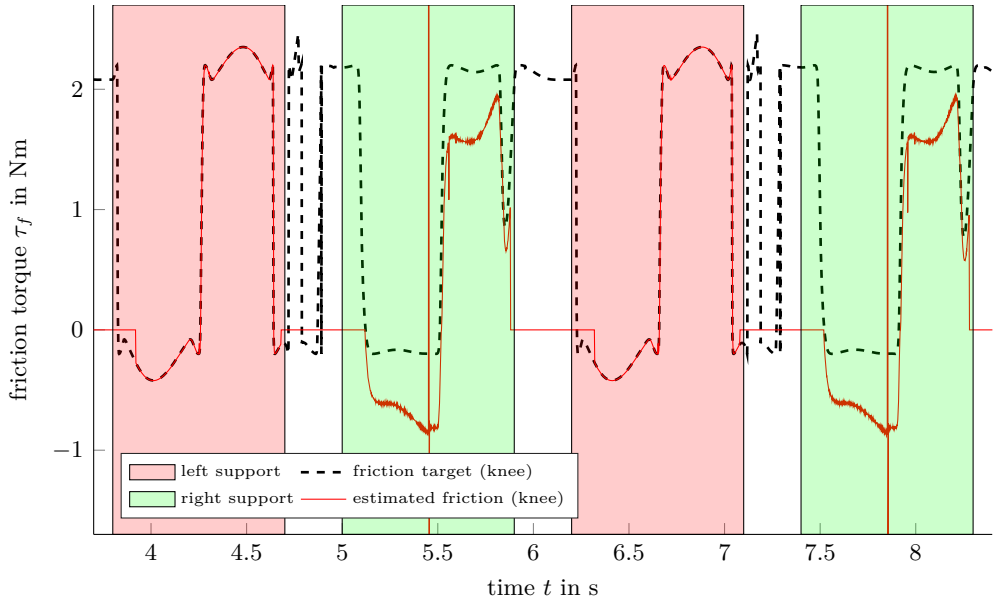

Figure 6.4: Friction estimation of the right knee in OpenHRP Simulation

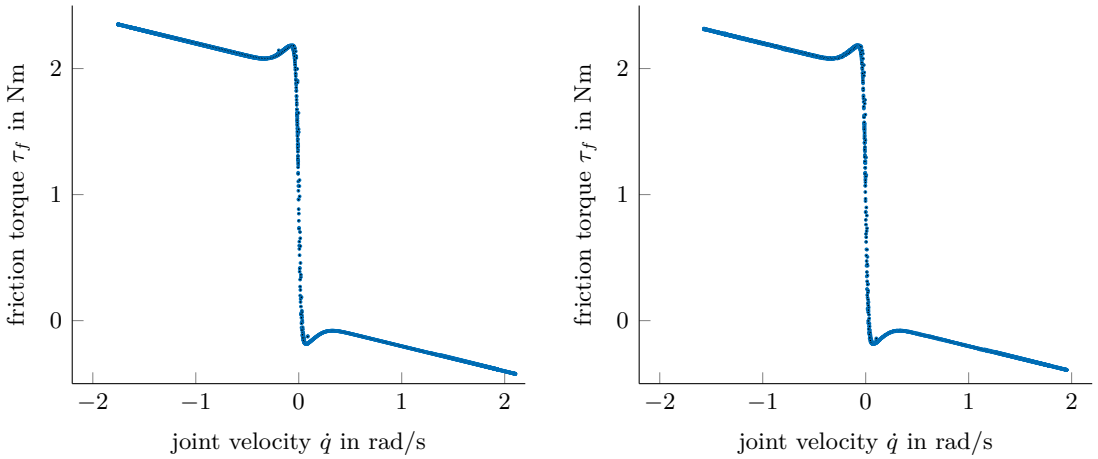

(a) friction in right knee only

(b) friction in all leg joints

Figure 6.5: OpenHRP friction estimation of the right knee in the leg's in swing phase with (a) friction applied to the right knee only and (b) friction applied to all leg joints

match the torque level of the individual joint and avoid oscillations caused by the controller due to high friction torques. The optimization can be formulated as

$$\hat{\mathbf{p}} = \min_{\mathbf{p}} \sum_{i=1}^{N} \left(\boldsymbol{\tau}_{f,mdl}(\dot{\mathbf{q}}, \mathbf{p}) - \boldsymbol{\tau}_{f,est}(\dot{\mathbf{q}}) \right)^2 , \tag{6.4}$$

where $\mathbf{p} \in \mathbb{R}^j$ is the vector of j friction model parameters. The solution to the curve fitting problem is obtained using a trust-region-reflective algorithm available in the Matlab optimization toolbox. The results are listed in Table 6.1 for TORO walking straight ahead. While walking straight, some of the joints are not experiencing high enough joint velocities to clear the Stribeck part of the friction curve. It is therefore not possible to

estimate the respecting parameters in that case. This can be improved by additionally walking sideways and increasing the step height and length. However, with larger steps, the control of the robot gets more challenging and signals increasingly more noisy. In Table 6.2 a compromise between larger steps to incorporate higher joint velocities and the prevention of overly noisy signals has been found. The step length accounts for 0.3 m forward and 0.25 m sideways. It can be observed that the parameter error can be significantly reduced if all joints cover a high enough velocity range to replicate all friction phenomena in the friction curve.

Table 6.1: Identified friction model parameters and corresponding error to the target value for TORO walking straight ahead (1-6: right leg, 7-12: left leg)

	joint	F_v	F_c	S	v_s	τ_{os}	a
target		0.2	0.8	0.2	0.2	0.8	40
	2 - hip pitch	0.1950	0.7528	0.1992	0.1988	0.7526	39.3728
	error [%]	2.50	0.37	0.40	0.60	0.35	1.57
	3 - hip yaw	0.2308	0.7403	0.2106	0.1967	0.7470	40.5316
	error [%]	15.40	1.29	5.30	1.65	0.40	1.33
	8 - hip pitch	0.1872	0.7581	0.2012	0.1849	0.7550	37.6777
	error [%]	6.40	1.08	0.60	7.55	0.67	5.81
	9 - hip yaw	0.0000	0.8234	0.1112	0.1799	0.7538	39.2904
	error [%]	100.00	9.79	44.40	10.05	0.51	1.77
target		0.2	1.0	0.2	0.2	1.0	40
	1 - hip roll	2.1435	0.4372	1.5603	0.1994	1.0037	41.3749
	error [%]	971.75	56.28	680.15	0.30	0.37	3.44
	4 - knee	0.1990	1.0017	0.1987	0.1966	0.9997	39.1141
	error [%]	0.50	0.17	0.65	1.70	0.03	2.21
	7 - hip roll	2.4518	0.5627	0.9846	0.1557	0.9954	41.2369
	error [%]	1125.90	43.73	392.30	22.15	0.46	3.09
	10 - knee	0.1984	1.0032	0.1974	0.1954	0.9991	38.7153
	error [%]	0.80	0.32	1.30	2.30	0.09	3.21
target		0.2	0.1	0.2	0.2	0.1	40
	5 - ankle roll	0.1881	0.1035	0.1649	0.1966	0.0995	39.787
	error [%]	5.95	3.50	17.55	1.70	0.50	0.53
	11 - ankle roll	0.1310	0.1220	0.0108	0.0864	0.1007	37.4309
	error [%]	34.50	22.00	94.60	56.80	0.70	6.42
target		0.2	0.2	0.2	0.2	0.2	40
	6 - ankle pitch	0.2000	0.2002	0.1999	0.2017	0.2005	39.5751
	error [%]	0.00	0.10	0.05	0.85	0.25	1.06
	12 - ankle pitch	0.2000	0.2002	0.2002	0.2013	0.2002	39.3951
	error [%]	0.00	0.10	0.10	0.65	0.10	1.51

Table 6.2: Identified friction model parameters and corresponding error to the target value for TORO walking both sideways and straight (1-6: right leg, 7-12: left leg)

	joint	F_v	F_c	S	v_s	τ_{os}	a
target		0.2	0.8	0.2	0.2	0.8	40
	2 - hip pitch	0.1985	0.7512	0.2028	0.1965	0.7515	40.4450
	error [%]	0.75	0.16	1.40	1.75	0.20	1.11
	3 - hip yaw	0.1807	0.7599	0.1870	0.1906	0.7476	40.3447
	error [%]	9.65	1.32	6.50	4.70	0.32	0.86
	8 - hip pitch	0.1970	0.7528	0.1997	0.1876	0.7510	41.0006
	error [%]	1.50	0.37	0.15	6.20	0.13	2.50
	9 - hip yaw	0.2193	0.7415	0.2140	0.2035	0.7518	40.0092
	error [%]	9.65	1.13	7.00	1.75	0.24	0.02
target		0.2	1.0	0.2	0.2	1.0	40
	1 - hip roll	0.1655	1.0135	0.1883	0.1957	1.0031	39.5902
	error [%]	17.25	1.35	5.85	2.15	0.31	1.02
	4 - knee	0.1999	1.0003	0.2049	0.1968	0.9996	36.8372
	error [%]	0.05	0.03	2.45	1.60	0.04	7.91
	7 - hip roll	0.1646	1.0183	0.1761	0.1992	0.9959	40.3043
	error [%]	17.70	1.83	11.95	0.40	0.41	0.76
	10 - knee	0.1998	1.0011	0.2036	0.1957	0.9996	36.5593
	error [%]	0.10	0.11	1.80	2.15	0.04	8.60
target		0.2	0.1	0.2	0.2	0.1	40
	5 - ankle roll	0.1991	0.1005	0.1960	0.1939	0.0995	39.8036
	error [%]	0.45	0.50	2.00	3.05	0.50	0.49
	11 - ankle roll	0.2010	0.0994	0.2060	0.2054	0.1004	39.6981
	error [%]	0.50	0.60	3.00	2.70	0.40	0.75
target		0.2	0.2	0.2	0.2	0.2	40
	6 - ankle pitch	0.1998	0.2003	0.1974	0.2009	0.2005	39.4428
	error [%]	0.10	0.15	1.30	0.45	0.25	1.39
	12 - ankle pitch	0.2002	0.2000	0.1990	0.2023	0.2004	39.5248
	error [%]	0.10	0.00	0.50	1.15	0.20	1.19

Chapter 7

Experimental Evaluation

As described in the previous Chapter, the friction torque applied in simulation can be accurately recovered. Unfortunately, in experiments, the identification method is exposed to real-world imperfection such as sensor noise, communication delays, modeling errors of robot inertia's and link and joint elasticities [6]. The experimental data is available in a log-format from which all necessary quantities of the friction estimation can be computed offline. The advantage of an offline friction estimation is that a zero phase filter can be applied to the desired signals which does not introduce a phase delay.

7.1 Filter design

Two filter types are presented in the following Section. The first is a symmetrical FIR filter designed specifically to minimize the 2-norm error of polynomials fitted locally to the data. The second is an IIR filter for which the zero phase property is obtained by the combination of forward and reverse filtering.

7.1.1 Savitzky-Golay filter

A least-squares polynomial smoothing, which is also known as Savitzky-Golay filter, is suggested to reduce noise and high-frequency oscillations while maintaining the shape and height of the low-frequency waveform [17]. The general idea of this lowpass filter is to fit a kth-order polynomial

$$p(n) = \sum_{i=0}^{k} a_i n^i \tag{7.1}$$

to a window of length $L = 2N + 1$ equally spaced data points $x[n]$ centered at $n = 0$ by the method of linear least squares.

The full system of equations for the L estimated data points $\hat{x}[n]$ can be written in terms of $p(n)$ as

$$\begin{bmatrix} \hat{x}[-n] \\ \vdots \\ \hat{x}[-1] \\ \hat{x}[0] \\ \hat{x}[1] \\ \vdots \\ \hat{x}[n] \end{bmatrix} = \begin{bmatrix} a_0 + a_1(-n) + a_2(-n)^2 + \cdots + a_k(-n)^k \\ \vdots \\ a_0 + a_1(-1) + a_2(-1)^2 + \cdots + a_k(-1)^k \\ a_0 + a_1(0) + a_2(0)^2 + \cdots + a_k(0)^k \\ a_0 + a_1(1) + a_2(1)^2 + \cdots + a_k(1)^k \\ \vdots \\ a_0 + a_1(n) + a_2(n)^2 + \cdots + a_k(n)^k \end{bmatrix} \tag{7.2}$$

and converted to matrix notation:

$$\hat{\mathbf{x}} = \begin{bmatrix} 1 & -n & (-n)^2 & \dots & (-n)^k \\ 1 & \vdots & \vdots & \iddots & \vdots \\ 1 & -1 & (-1)^2 & \dots & (-1)^k \\ 1 & 0 & 0 & \dots & 0 \\ 1 & 1 & 1^2 & \dots & 1^k \\ 1 & \vdots & \vdots & \ddots & \vdots \\ 1 & n & n^2 & \dots & n^k \end{bmatrix} \begin{bmatrix} a_0 \\ \vdots \\ a_k \end{bmatrix} = \mathbf{Ta}. \tag{7.3}$$

A optimization problem that minimizes the weighted square of the error $(\hat{\mathbf{x}} - \mathbf{x})$ is formulated as

$$\min_{\mathbf{a}} \frac{1}{2}(\mathbf{a}^T\mathbf{T}^T - \mathbf{x}^T)\mathbf{W}(\mathbf{Ta} - \mathbf{x}). \tag{7.4}$$

The solution is given by the $\mathbf{W}$-weighted pseudo-inverse of $\mathbf{T}$:

$$\mathbf{a} = \left(\mathbf{T}^T\mathbf{WT}\right)^{-1}\mathbf{T}^T\mathbf{Wx}, \tag{7.5}$$

with $\mathbf{W}$ being a diagonal matrix containing the weights $\mathbf{w}$ of the individual data points. Here, the matrix $\mathbf{W}$ is the identity matrix, but other distributions are possible, e.g. a symmetrical bell-shaped curve. It is important to note that the weights must also be symmetric about the central point to retain the zero-phase property of the filter.

Multiplying $\mathbf{T}$ from the left yields the Savitzky-Golay estimates:

$$\hat{\mathbf{x}} = \mathbf{T}\left(\mathbf{T}^T\mathbf{WT}\right)^{-1}\mathbf{T}^T\mathbf{Wx} = \mathbf{Bx}. \tag{7.6}$$

Only the central point of the estimated data $\hat{\mathbf{x}}$ is retained. It is given by evaluating $p(n)$ at the central point $n = 0$, which is equal to the 0th polynomial coefficient:

$$y = \hat{x}[0] = p(0) = a_0. \tag{7.7}$$

An output value $y[t]$ for every data point in a sample is calculated by moving the approximation interval across the input signal $x[t]$. At each point, a polynomial is fitted

to the window of L data points and evaluated at the central location. Generally, the filter window need not be symmetrical about the central point, which can be useful for approximating the first and final n values of the filtered signal. However, this leads to a nonlinear-phase filter and is neglected in this work as there are always enough (more than n) data points at the beginning and end of the signal which are excluded in the friction estimation. Therefore, the filtered data is only calculated for the part of the signal with enough data points to the left and right to assure a symmetrical window about the center point. For this part, a more convenient computation method is introduced in the following.

Savitzky and Golay [16] found that the process of fitting a polynomial to a window of L sample points and evaluating the resulting polynomial at a single point within the window is equivalent to determining the weighted sum of the L sample points with a fixed set of convolution parameters. This set of parameters is the impulse response $h[n]$ of the filter. It can be calculated once for a window of length L, a polynomial of order k and weighing factors $\mathbf{w}$. The output values $y[t]$ can then be computed by the discrete convolution:

$$y[t] = \sum_{m=-N}^{N} h[m]x[t-m]. \tag{7.8}$$

For the calculation of $\hat{x}[0]$, the central value of $\hat{\mathbf{x}}$, only the center row of $\mathbf{B}$ in equation (7.6) is needed. It is independent of the input data and represents the impulse response $h[n]$ for a certain choice of L, k and $\mathbf{w}$. By convolution with an input signal, it yields the filtered output signal in a single operation. Again, the signal edges need to be treated differently if correct results are required here. For this thesis, however, the steady-state part of the filtered signal achieved by the above convolution is sufficient.

Conveniently the numerical derivatives of the filtered signal can be readily calculated by this method. For this, the polynomial is replaced by its desired derivative and the impulse response scaled by powers of the finite time step.

From a frequency-domain point of view, the cutoff frequency of the Savitzky-Golay filter depends on the window length L, polynomial order k and weighting vector $\mathbf{w}$. This is further discussed in Section 7.2 in comparison to the butterworth filter.

7.1.2 Butterworth filter

An alternative to the above filter design is to use a central derivative algorithm (e.g. eq. (6.2)) to obtain the acceleration and pass the signal through an IIR lowpass butterworth filter in both the forward and backward direction. In this way a non-causal zero phase filter is achieved. This can readily be executed using the *filtfilt* function in Matlab. The butterworh filter is designed to have a maximally flat frequency response in the pass band, which is desirable to retain the shape and magnitude of the low frequencies. In order to tune the lowpass filter, a Fast Fourier Transform (FFT) is performed on the estimated acceleration. Calculated by the forward dynamics model and therefore less disturbed, it yields a good approximation for the cutoff frequency of the butterworth filter. Figure 7.1 shows the FFT of the estimated acceleration of the knee and the hip pitch joint to be exemplary for all other joints. There are no distinguishable frequency peaks beyond 10 Hz, which will be the cutoff frequency assumption for the measured

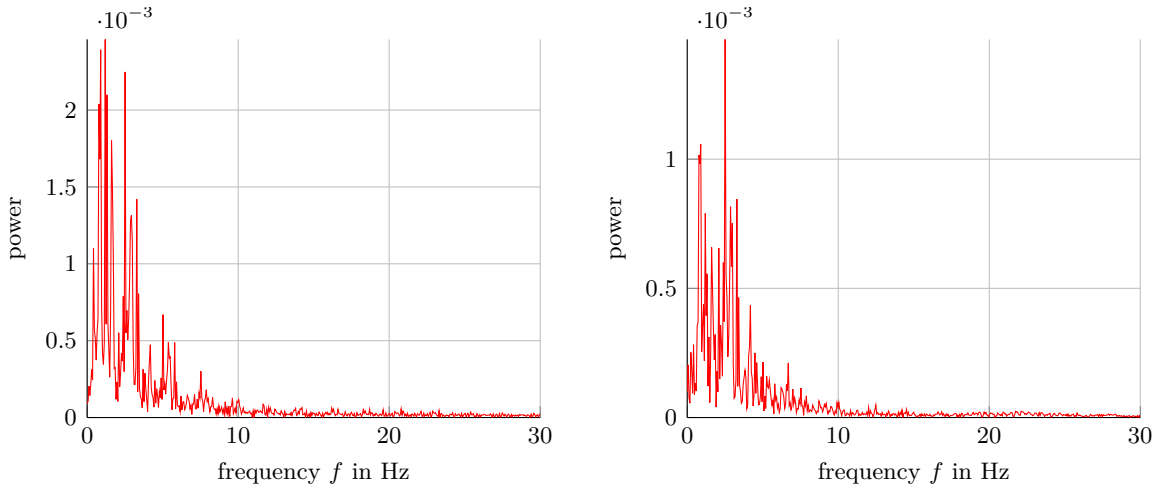

(a) FFT knee acceleration

(b) FFT hip pitch acceleration

Figure 7.1: Fast Fourier Transform of the estimated joint acceleration of (a) knee and (b) hip pitch joint

acceleration filter. With a sampling rate of 1000 Hz, the normalized cutoff frequency is equal to $\omega_c = 0.02 \times \pi \frac{\text{rad}}{\text{s}}$.

7.2 Experimental results

Due to considerably higher noise and vibration levels in the experimental data, a trade-off between minimum distortion of the desired signal and maximum noise attenuation needs to be found. In order to investigate the effect of the filter on the friction estimation, it is first applied to simulation data for which the target friction is known. Figure 7.2 shows the estimated friction of the right knee (undistorted in Fig. 6.5a) for various filter designs. With decreasing cutoff frequency the filter starts to deform the lower frequencies and especially the Stribeck curve is affected. The two filter designs in Fig. 7.2c and Fig. 7.2d have a comparable cutoff frequency and display a very similar deformation of the frequencies in the Stribeck part of the friction curve. However, the Savitzky-Golay filter preserves the shape of the even lower frequencies better than the butterworth filter. This can be seen by the convergence of the Savitzky-Golay-filtered friction to the friction target for higher joint velocities.

Figure 7.3 shows the estimated and measured acceleration of the right knee joint during a step with the right leg in the swing phase. It is displayed for a simulation (Fig. 7.3a) and an experiment (Fig. 7.3b) with the same walking parameters, i.e., double and single support time and step-length and height. The single support time measures the full 0.8 s, but the calculation is only performed for the central 0.6 s due to spikes in the acceleration during lift-off and touch-down of the foot.

In the experiment, a significantly higher acceleration estimate can be recorded compared to simulation, whereas its shape shows similarities. A possible approach to explain higher acceleration estimates in the experiment is that greater tracking errors result in higher desired/commanded torques, which contribute to the acceleration estimate. If the joints of the real robot, however, are stuck in friction, they cannot follow this fast

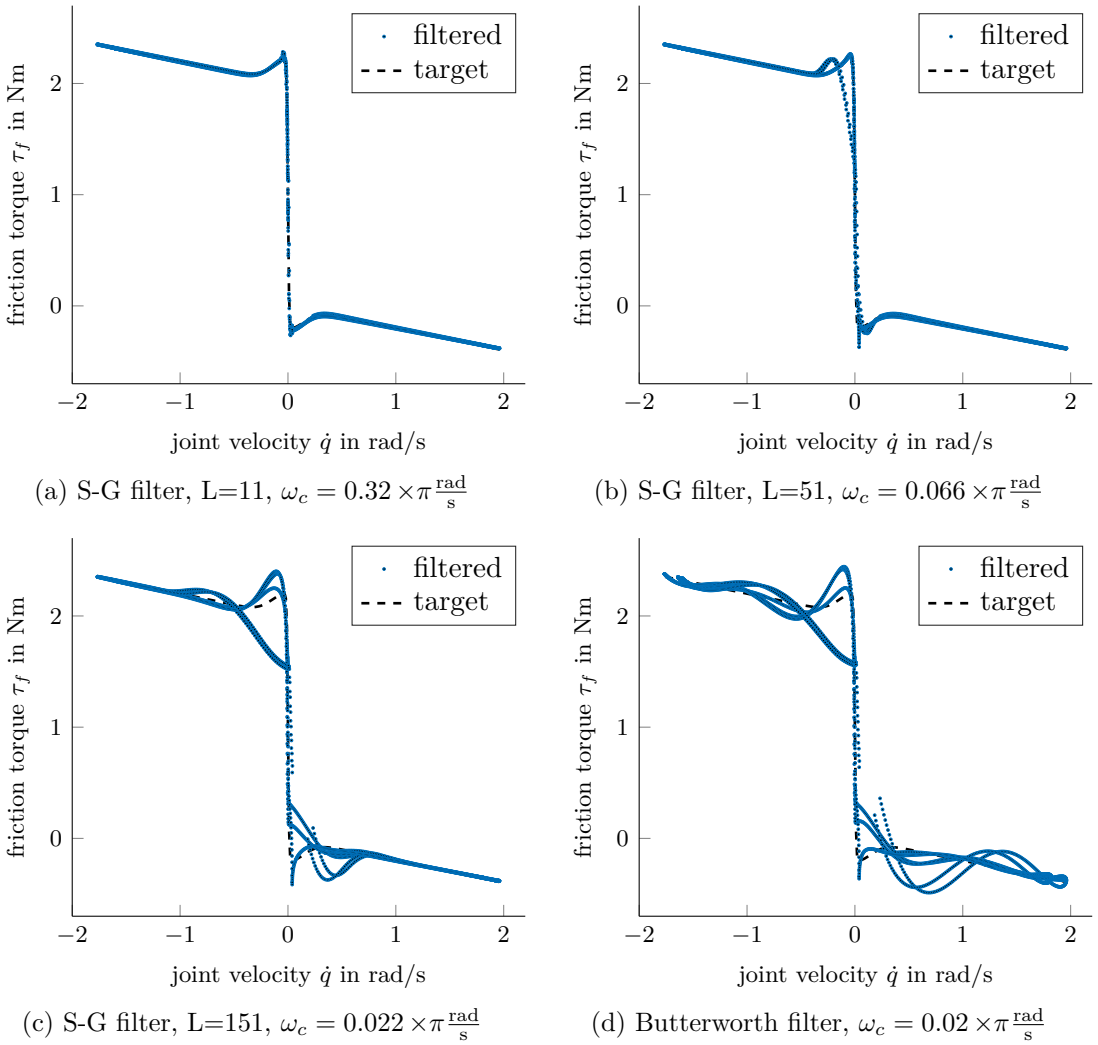

(a) S-G filter, L=11, $\omega_c = 0.32 \times \pi \frac{\text{rad}}{\text{s}}$

(b) S-G filter, L=51, $\omega_c = 0.066 \times \pi \frac{\text{rad}}{\text{s}}$

(c) S-G filter, L=151, $\omega_c = 0.022 \times \pi \frac{\text{rad}}{\text{s}}$

(d) Butterworth filter, $\omega_c = 0.02 \times \pi \frac{\text{rad}}{\text{s}}$

Figure 7.2: Filtered estimated friction torque of the right knee with unweighted Savitzky-Golay filter of order 4 and varying window length (a)-(c) and 6th-order lowpass butterworth filter applied in forward and reverse direction (d)

recovery strategy. Partly as a consequence, the measured and filtered acceleration is smaller in the experiment than in simulation. Thus far, simply a higher friction torque in the experiment can be supposed. However, there are more subtle differences that prevent the friction curve, i.e., when plotted over velocity, from looking much alike. Figure 7.4 illustrates that, if the dynamic model of the robot is exact, the difference between estimated and measured joint acceleration $\Delta\ddot{q}$ and joint velocity $\dot{q}_{msr}$ have always opposite signs. This must be true as the frictional torque $\boldsymbol{\tau}_f = \mathbf{M}_{mod}\Delta\ddot{\mathbf{q}}_{tc}$, with $\mathbf{M}_{mod}$ being positive definite, dissipates energy. The power extracted by friction from the system is negative:

$$P_f = \dot{\mathbf{q}}_{tc}^T \boldsymbol{\tau}_f < 0. \tag{7.9}$$

The velocity and acceleration difference graphs in Fig. 7.4a intersect exactly at zero and have opposite signs everywhere else, which guarantees that the friction torque plotted over velocity also intersects the origin and the extracted power is negative. For the

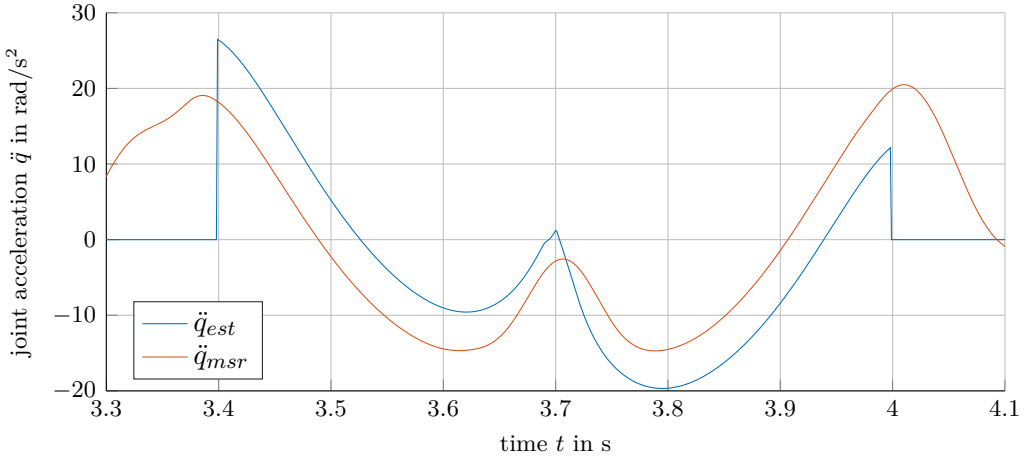

(a) Simulation data: $\ddot{q}_{msr}$ filtered with S-G filter with window length $L = 151$

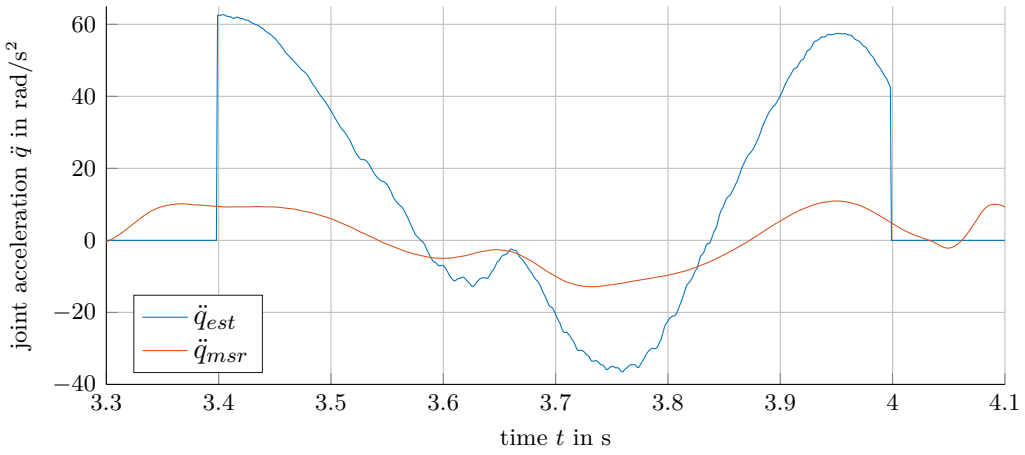

(b) Experimental data: $\ddot{q}_{msr}$ filtered with S-G filter with window length $L = 151$

Figure 7.3: Comparison of estimated and measured acceleration for the right knee in simulation (a) and experiment (b)

experimental data in Fig. 7.4b, the intersections of the two graphs do not occur at zero and there exist periods for which the estimated friction generates positive power, which conflicts with the energy conservation principle and is therefore incorrect. Additionally, the unfiltered acceleration is displayed in both figures. It can be observed that the unphysical friction torque estimates do not originate from filtering, as the intersections of the graphs are not significantly changed by the Savitzky-Golay filter for both simulation and experiment. Additionally to Fig. 7.2, which showed that the low frequencies were not affected by the filter, this suggests that the erroneous friction torque must be caused otherwise, for instance by modeling errors of inertia parameters.

In order to investigate the influence of inaccurate inertia parameters in simulation, the friction torque is calculated with slightly varying mass matrices. In particular, the mass matrices of the robot's i individual rigid bodies are modified to approximate an inexact dynamic model for the friction estimation, whereas the mass matrices for the forward dynamics, that is the simulation, remain unchanged. In the unconstrained case, a single rigid body has 6 degrees of freedom (3 Cartesian positions and 3 rotations) resulting in

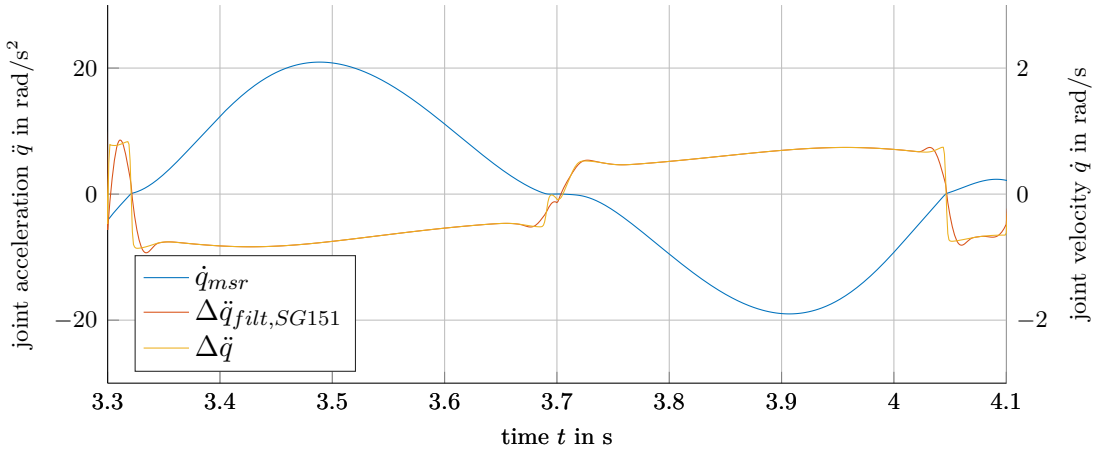

(a) Simulation

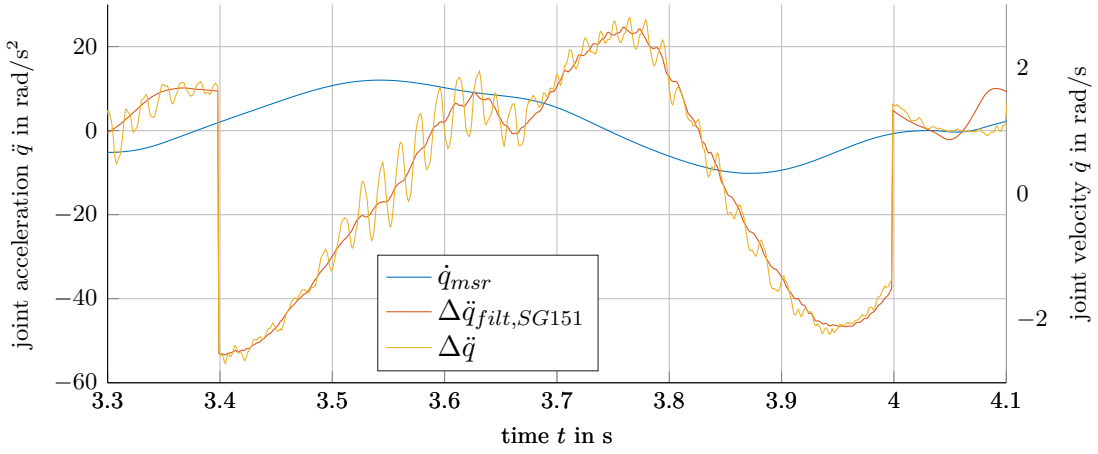

(b) Experiment

Figure 7.4: Acceleration difference and velocity of the right knee in simulation (a) and experiment (b)

an individual inertia matrix $\mathbf{M}_i \in \mathbb{R}^{6\times6}$. In a first approximation, the elements of each mass matrix $\mathbf{M}_i$ are scaled equally.

Figure 7.5 shows the friction estimation for the right knee calculated with different scaling factors. The friction curve is truncated in order to avoid the noisy lift-off and touch-down phase of the leg and therefore the decreasing velocity branch does not return to the origin. It can be observed that the friction curve is shifted down for lower inertia and up for higher inertia. The friction torque between different steps of the robot varies slightly and branches for increasing and decreasing velocities start to separate, although the general shape of the friction curve is mostly preserved. This shift due to inaccurate inertia, however, conflicts with the displacement of the friction curve as a result of torque offset induced by an erroneous sensor calibration routine.

To separate the sensitivity towards modeling errors of mass and moment of inertia, the eigendecomposition of matrix $\mathbf{M}_i$ is calculated and only the eigenvalues corresponding to either mass or moment of inertia are scaled. The matrix is then transformed back to its original basis. By modifying only the mass properties of the individual rigid bodies very similar results as in Fig. 7.5 are obtained, as the mass corresponds to the dominant

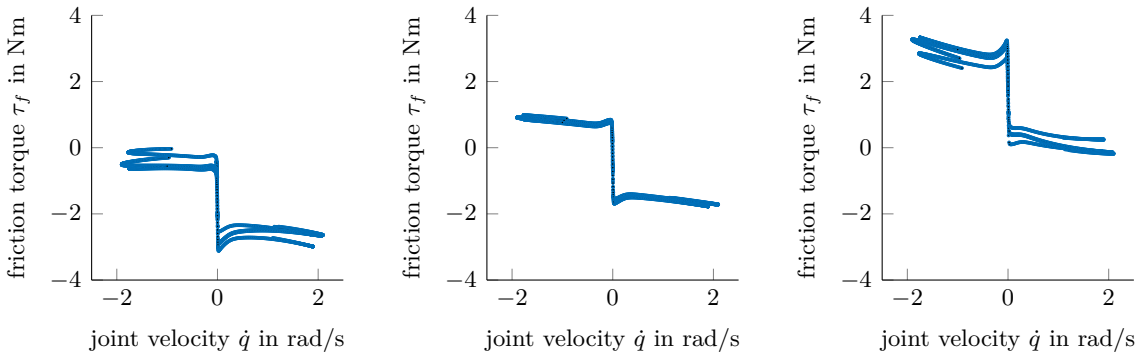

(a) $0.8 * \mathbf{M}_i$ (b) $0.95 * \mathbf{M}_i$ (c) $1.2 * \mathbf{M}_i$

Figure 7.5: Friction estimation with equally scaled individual rigid body mass matrices $\mathbf{M}_i$

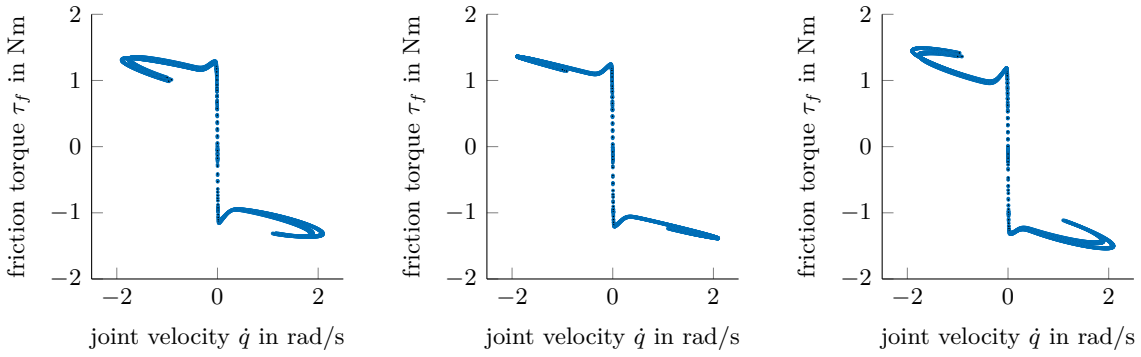

(a) $0.8 * \mathbf{I}_i$ (b) $0.95 * \mathbf{I}_i$ (c) $1.2 * \mathbf{I}_i$

Figure 7.6: Friction estimation with equally scaled principal moments of inertia $\mathbf{I}_i$ of the individual rigid body mass matrices $\mathbf{M}_i$

eigenvalues of matrix $\mathbf{M}_i$. Since the mass of a rigid body can be precisely measured and compared to the model, significant mass modeling errors are unrealistic (except for deviation of the center of gravity). The results of modified inertia properties are shown in Fig. 7.6. The vertical displacement of the friction curve is no longer present, yet the separation for increasing and decreasing velocities is more pronounced.

A similar friction curve is discovered for some joints in the experiment with the real robot. In Fig. 7.8 the friction torques obtained from experimental data for the right knee and ankle pitch joint are shown. Both friction curves exhibit separate branches for increasing and decreasing velocity similar to the simulation. The results for the right knee in Fig. 7.7a are additionally shifted up, which can be caused by either a torque offset or a mass modeling error. Due to real-world imperfections, both plots display unphysical friction torques, which would generate positive power. It can be concluded, that an exact friction calculation relies strongly on an accurate dynamical model of the robot.

For other joints the separation of the friction curve for increasing and decreasing velocities is not as pronounced. Nevertheless, despite filtering the influence of real-world

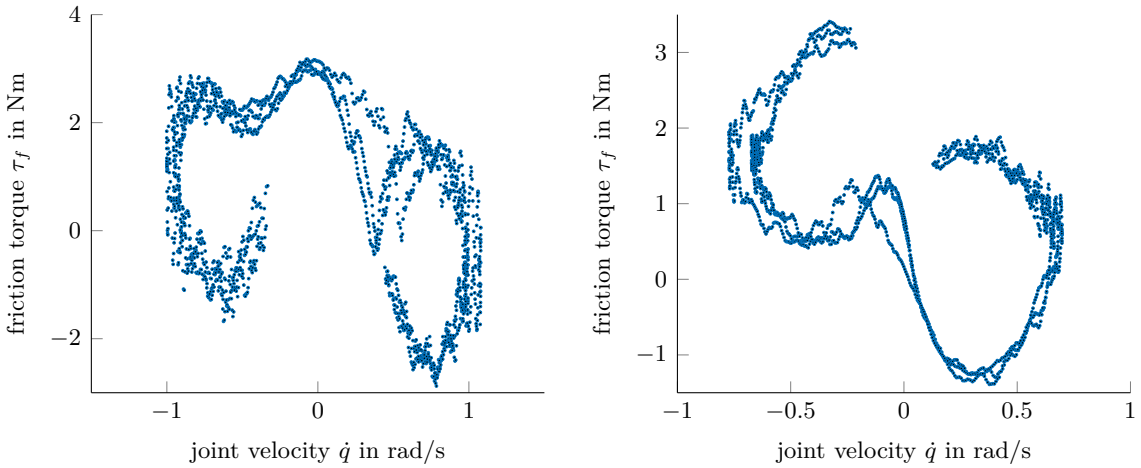

(a) Right knee joint (b) Right ankle pitch joint

Figure 7.7: Friction torque estimation for the right knee (a) and ankle pitch (b) joints in the experiment

imperfections like noise and vibration is still present, especially for the left hip pitch joint in Fig. 7.8b. For these joints, the difference between the right and the left side is apparent, although the same filter parameters are used. The ankle roll joint shown in Fig. 7.8a is for the most part unaffected by inertia modeling errors because the mass and moment of inertia of the foot are small and it is not influenced by other joints. In general, this would also apply to the ankle roll joint, but its actuator is mounted under the knee and additionally affected by the inertia and inaccuracy of the parallel bar mechanism.

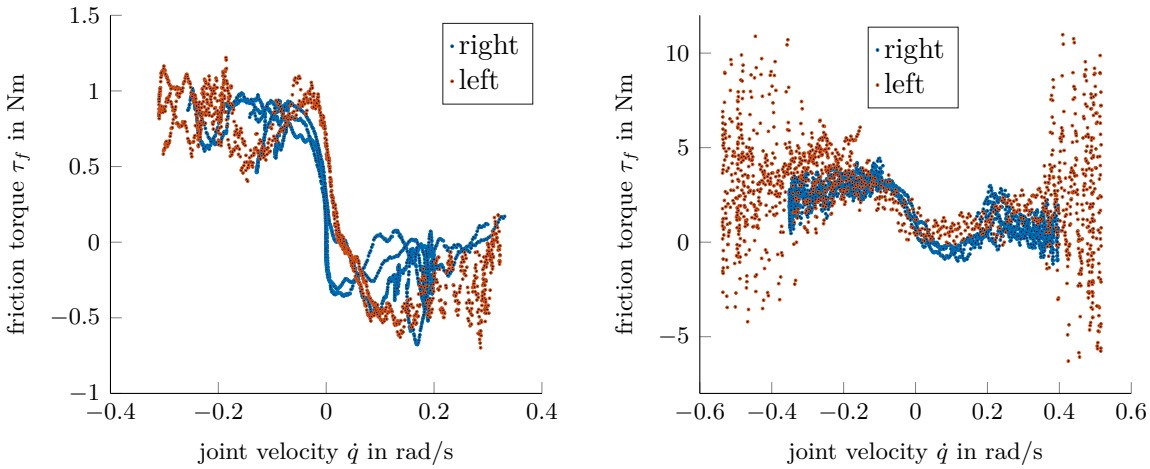

(a) Ankle roll joints (b) Hip pitch joints

Figure 7.8: Friction torque estimation for ankle roll (a) and hip pitch (b) joints in experiment

7.3 Discussion

The joint friction identification of the real robot is restricted by the real-world imperfections described in the previous Section. Since the method relies on the difference of measured and estimated joint acceleration, already high noise and vibration levels are increased by the second numerical time derivative of the joint positions. This can largely be compensated by the suggested filter designs.

Other phenomena limit the performance of the friction estimation to a greater extend by producing a frictional torque that generates positive power, which violates the energy conservation principle. It has been shown that these unphysical friction torques appear also in a simulation with an imprecise inertia model of the robot. Furthermore, the observed separation of the friction curve for increasing and decreasing velocities arises similarly in the simulation with an inexact model. This suggests, that the unphysical results for the experimental data originate from an insufficiently accurate inertia model although other causes, like unmodeled temperature and load dependency of the friction torque and sensor decalibration during the experiment cannot be completely excluded.

With prevailing uncertainty in the friction torque estimation, a parameter identification as described in Section 6.2.2 is not beneficial. An identification of the dynamic parameters of the robot, like inertia and friction, as described in Section 2.4 should be performed. The obtained results can be compared to the existing inertia model and improved if needed. With a more accurate dynamic model, the friction estimation described in this work should be repeated to examine if the unphysical friction torque estimates can be eliminated. When successful, the described parameter identification can be conducted and the resulting friction model used for friction compensation to improve the performance of the robot.

Chapter 8

Conclusion and Outlook

In this work a whole-body joint friction estimation method based on the acceleration difference between measured acceleration derived via numerical differentiation of joint positions and an estimated acceleration calculated through the constraint dynamic equations of the robot is developed.

At first, related work and an overview of commonly used friction models in robotics were presented. The mechanical design of the humanoid robot TORO has been outlined briefly and the dynamic model of walking robots was introduced. In Chapter 5 the whole body friction estimation method was derived in consideration of contact constraints imposed on the robot. In the subsequent Chapter, the obtained method was evaluated in simulation by both directly solving the constraint forward dynamics and the use of an external simulation within the OpenHRP software platform. Different support conditions and numerical differentiation schemes and their influences on the friction estimation have been investigated. A parameter identification via non-linear least-squares optimization has been performed to validate the performance of the friction estimation in different walking conditions. For the use of experimental data, different filter designs have been examined to find a compromise between minimum distortion of the signal and maximum noise/vibration attenuation. Finally, the experimental results were discussed.

In the simulation, it was shown that if the dynamic model of the robot is sufficiently accurate, the friction estimation returns reliable results. Nevertheless, real-world imperfections like sensor noise, vibrations and inaccurate inertia modeling or merely the error introduced by numerical differentiation expose different sensitivities of the estimation method. It is found that reliable results can be obtained in simulation for all joints by calculating the joint friction torque in the leg's swing phase. The friction estimation in the experiment is shown to be limited by real-world imperfections.

In future work, the derived friction estimation method should be repeated with an improved inertia model of the robot to investigate its influence on the friction torque estimation of the experimental data. Furthermore, a direct dynamic parameter estimation as described in Section 2.4 can be performed to validate the existing inertia model and obtain an estimate of Coulomb and viscous friction parameters from a different approach.

List of Figures

List of Tables

References

[1] B. Armstrong-Hélouvry, P. Dupont, and C. C. de Wit. A survey of models, analysis tools and compensation methods for the control of machines with friction. *Automatica*, 30(7):1083–1138, 1994. ISSN 0005-1098. doi: 10.1016/0005-1098(94)90209-7.

[2] J. Baur, S. Dendorfer, J. Pfaff, C. Schutz, T. Buschmann, and H. Ulbrich. Experimental friction identification in robot drives. In *2014 IEEE International Conference on Robotics and Automation (ICRA)*, pages 6006–6011. IEEE, 31.05.2014 - 07.06.2014. ISBN 978-1-4799-3685-4. doi: 10.1109/ICRA.2014.6907744.

[3] C. Canudas de Wit, H. Olsson, K. J. Astrom, and P. Lischinsky. A new model for control of systems with friction. *IEEE Transactions on Automatic Control*, 40(3): 419–425, 1995. ISSN 00189286. doi: 10.1109/9.376053.

[4] A. de Luca, A. Albu-Schaffer, S. Haddadin, and G. Hirzinger. Collision detection and safe reaction with the dlr-iii lightweight manipulator arm. In *Proceedings of the 2006 IEEE/RSJ International Conference*. IEEE, 2006. doi: 10.1109/IROS.2006.282053.

[5] J. Englsberger, A. Werner, C. Ott, B. Henze, M. A. Roa, G. Garofalo, R. Burger, A. Beyer, O. Eiberger, K. Schmid, and A. Albu-Schaffer. Overview of the torque-controlled humanoid robot toro. In *2014 IEEE-RAS International Conference on Humanoid Robots*, pages 916–923. IEEE, 18.11.2014 - 20.11.2014. ISBN 978-1-4799-7174-9. doi: 10.1109/HUMANOIDS.2014.7041473.

[6] J. Englsberger, G. Mesesan, A. Werner, and C. Ott. Torque-based dynamic walking - a long way from simulation to experiment. In *2018 IEEE International Conference on Robotics and Automation (ICRA)*, pages 440–447. IEEE, 21.05.2018 - 25.05.2018. ISBN 978-1-5386-3081-5. doi: 10.1109/ICRA.2018.8462862.

[7] L. Freidovich, A. Robertsson, A. Shiriaev, and R. Johansson. Lugre-model-based friction compensation. *IEEE Transactions on Control Systems Technology*, 18(1): 194–200, 2010. ISSN 1063-6536. doi: 10.1109/TCST.2008.2010501.

[8] M. Gautier. Dynamic identification of robots with power model. In *1997 IEEE International Conference On Robotics And Automation*. IEEE, 1997. doi: 10.1109/ROBOT.1997.619069.

[9] P. Hamon, M. Gautier, and P. Garrec. New dry friction model with load- and velocity-dependence and dynamic identification of multi-dof robots. In *2011 IEEE International Conference on Robotics and Automation*, pages 1077–1084. IEEE, 09.05.2011 - 13.05.2011. ISBN 978-1-61284-386-5. doi: 10.1109/ICRA.2011.5980126.

[10] I. Hashlamon and K. Erbatur. Joint friction estimation for walking bipeds. *Robotica*, 34(7):1610–1629, 2016. ISSN 0263-5747. doi: 10.1017/S0263574714002471.

[11] F. Kanehiro, K. Fujiwara, S. Kajita, K. Yokoi, K. Kaneko, H. Hirukawa, Y. Nakamura, and K. Yamane. Open architecture humanoid robotics platform. In *Proceedings 2002 IEEE International Conference on Robotics and Automation (Cat. No.02CH37292)*, pages 24–30. IEEE, 11-15 May 2002. ISBN 0-7803-7272-7. doi: 10.1109/ROBOT.2002.1013334.

[12] L. Le Tien, A. Albu-Schaffer, A. de Luca, and G. Hirzinger. Friction observer and compensation for control of robots with joint torque measurement. In *2008 IEEE/RSJ International Conference on Intelligent Robots and Systems*, pages 3789–3795. IEEE, 22.09.2008 - 26.09.2008. ISBN 978-1-4244-2057-5. doi: 10.1109/IROS.2008.4651049.

[13] M. Iskandar and S. Wolf. Dynamic friction model with thermal and load dependency: modeling, compensation, and external force estimation. In *2019 International Conference on Robotics and Automation (ICRA)*, pages 7367–7373, 2019. ISBN 2577-087X. doi: 10.1109/ICRA.2019.8794406.

[14] H. Olsson. *Control Systems with Friction*. PhD thesis, Department of Automatic Control, Lund Institute of Technology, 1996.

[15] P. J. Olver. *Introduction to Partial Differential Equations*. Undergraduate Texts in Mathematics. Springer International Publishing, Cham and s.l., 2014. ISBN 9783319020990. doi: 10.1007/978-3-319-02099-0.

[16] A. Savitzky and M. J. E. Golay. Smoothing and differentiation of data by simplified least squares procedures. *Analytical Chemistry*, 36(8):1627–1639, 1964. ISSN 0003-2700. doi: 10.1021/ac60214a047.

[17] R. Schafer. What is a savitzky-golay filter? [lecture notes]. *IEEE Signal Processing Magazine*, 28(4):111–117, 2011. ISSN 1053-5888. doi: 10.1109/MSP.2011.941097.

[18] S. Wolf and M. Iskandar. Extending a dynamic friction model with nonlinear viscous and thermal dependency for a motor and harmonic drive gear. In *2018 IEEE International Conference on Robotics and Automation (ICRA)*, pages 783–790. IEEE, 21.05.2018 - 25.05.2018. ISBN 978-1-5386-3081-5. doi: 10.1109/ICRA.2018.8460613.